CWP-905

Seismic source mechanism imaging

Ivan Lim Chen Ning & Paul Sava
Center for Wave Phenomena, Colorado School of Mines

ABSTRACT

Wavefield-based solutions are robust and facilitate straightforward seismic source parameter estimation. The potential to access multicomponent stress and particle displacement data through new technology such as distributed acoustic sensing (DAS) allows us to formulate the source mechanism imaging problem using full anisotropic elastic wavefields. We propose a method that enables us to obtain the source location and mechanism simultaneously, without the need for lengthy iterative inversion. Our technique requires knowledge of the medium model parameters (also a requirement for any other wavefield-based method) for reverse-time wavefield extrapolation, and the source wavelet (which can be reasonably well estimated) for the imaging condition. The source location and mechanism are inherently embedded in our imaging process. For high-resolution imaging, least-squares solutions diminish artifacts due to limited receiver coverage and illumination. We test our approach on multiple 3D numerical experiments using various combinations of source mechanisms, in order to demonstrate its capability to recover the source parameters.

Key words: moment tensor, seismic imaging

1 INTRODUCTION

Seismic source imaging is widely used in seismology, especially for earthquake and microseismic monitoring and characterization. The source parameters such as location, excitation time, and focal mechanism are of great interest as they provide information about reservoirs subject to hydraulic fracturing (Baig and Urbancic, 2010). The source information also allows us to quantify the extent (width and distance) of the induced fractures. Through the source mechanism, we can infer the fracture orientation that enables strategic decisions for borehole placement to improve reservoir production (Maxwell et al., 2010).

The source parameters can be obtained through waveform tomography for simultaneous multi-source parameter inversion based on the amplitude and phase information of the recorded data. Waveform tomography utilizes adjoint wavefields simulated by reverse time extrapolation (Tromp et al., 2005; Kim et al., 2011; Jarillo Michel and Tsvankin, 2014, 2015, 2017). Alternatively, one can use reverse time imaging for source location (Artman et al., 2010; Li et al., 2017), or can adopt optimization-based source imaging for reduced truncation artifacts and higher resolution (Fukahata et al., 2013; Bazargani and Snieder, 2015; Nakahara and Haney, 2015). Chambers et al. (2014) investigate the use of diffraction stacking to obtain the source mechanism through imaging. Kawakatsu and Montagner (2008) as well as Gharti et al. (2011) outline the theory of reverse time imaging to provide an approximate estimate of the seismic source mechanism by conventional amplitude-based inversions, i.e., using the Greens functions. Similarly, Montagner et al. (2012) demonstrate the use of reverse time wavefields to retrieve the source mechanism (moment tensor) from long period waves.

In this paper, we propose to use reverse-time wavefield extrapolation to obtain the seismic source mechanism through imaging without the need for lengthy iterative inversion. Our method requires both stress and particle displacement data in order to reconstruct accurately subsurface wavefields in heterogeneous and anisotropic media. Although stress data are not commonly acquired, we frame our method in the context of new acquisition technologies such as distributed acoustic sensing (DAS) that measures strain along optical fibers. We can obtain multicomponent DAS strain measurements using novel optical fiber configurations (Lim Chen Ning and Sava, 2016, 2018, 2017). Assuming knowledge of the Earth's material properties surrounding the optical fiber, we can compute stress from strain via conventional constitutive relations (Aki and Richards, 2002). Without loss of generality, we can formulate our imaging approach with either stress or particle displacement data as special cases. The source image contains information about its source location and mechanism.

We demonstrate the proposed imaging process using

3D numerical simulations that mimic passive seismic experiments. We test our algorithm with multiple source mechanism consisting of moment tensor or body force sources. The tested acquisition geometry includes both spherical receiver distributions for full aperture analysis, as well as surface receivers to emulate practical microseismic observation arrays.

2 THEORY

We describe elastic-wave propagation using the second-order partial differential equations consisting of both stress $\underline{\mathbf{t}}\mathbf{u}(\mathbf{x},t)$ tensor and particle displacement $\mathbf{u}\mathbf{u}(\mathbf{x},t)$ vector wavefields (Aki and Richards, 2002)

$$\rho\,\frac{\partial^2\mathbf{u}}{\partial t^2} = \nabla\cdot\underline{\mathbf{t}} + \mathbf{f}\,, \tag{1}$$

where $\mathbf{x}$ and t denote space and time, respectively. $\rho(\mathbf{x})$ is the density and $\mathbf{f}(\mathbf{x},t)$ is the external volume force. Under the assumption of linear elasticity the stress $\underline{\mathbf{t}}(\mathbf{x},t)$ is related to strain $\underline{\mathbf{e}}(\mathbf{x},t)$ through the constitutive relation

$$\underline{\mathbf{t}} = \underline{\underline{\mathbf{c}}}\,\underline{\mathbf{e}} + \underline{\mathbf{m}}\,, \tag{2}$$

where $\underline{\mathbf{m}}(\mathbf{x},t)$ is the seismic moment tensor source acting as stress perturbation. The relation between the strain $\underline{\mathbf{e}}(\mathbf{x},t)$ tensor and particle displacement $\mathbf{u}(\mathbf{x},t)$ is

$$\begin{aligned}\underline{\mathbf{e}} &= \frac{1}{2}\left\{\nabla\mathbf{u} + (\nabla\mathbf{u})^{\intercal}\right\}\\ &= \mathbf{H}\,\mathbf{u}\,,\end{aligned} \tag{3}$$

where the operator $\mathbf{H}$ captures the geometric relation between strain and particle displacement. We express the seismic moment tensor source as

$$\underline{\mathbf{m}} = \mathrm{s}^{\mathbf{m}}\,\mathbf{M}\,, \tag{4}$$

where $\mathbf{M}(\mathbf{x})$ is a unitless matrix that determines the magnitude of the moment tensor source. $\mathrm{s}^{\mathbf{m}}(t)$ denotes the moment tensor source wavelet with units of stress (force per unit area). Similarly, we express the body force vector as

$$\mathbf{f} = \mathrm{s}^{\mathbf{f}}\,\mathbf{F}\,, \tag{5}$$

where $\mathbf{F}(\mathbf{x})$ is a unitless vector that determines the magnitude of the body force source. $\mathrm{s}^{\mathbf{f}}(t)$ represents the body force source wavelet with units of force density (force per unit volume). We can interpret $\mathbf{M}(\mathbf{x})$ and $\mathbf{F}(\mathbf{x})$ as images that show the source location and its associated mechanism. Following the notations in equations 4 and 5, we can define the moment tensor source term in matrix form as

$$\begin{bmatrix}\underline{\mathbf{m}}_0\\ \underline{\mathbf{m}}_1\\ \underline{\mathbf{m}}_2\\ \vdots\end{bmatrix} = \begin{bmatrix}\mathrm{s}_0^{\mathbf{m}}\\ \mathrm{s}_1^{\mathbf{m}}\\ \mathrm{s}_2^{\mathbf{m}}\\ \vdots\end{bmatrix}\Big[\,\mathbf{M}\,\Big] \tag{6}$$

and the corresponding body force source term as

$$\begin{bmatrix}\mathbf{f}_0\\ \mathbf{f}_1\\ \mathbf{f}_2\\ \vdots\end{bmatrix} = \begin{bmatrix}\mathrm{s}_0^{\mathbf{f}}\\ \mathrm{s}_1^{\mathbf{f}}\\ \mathrm{s}_2^{\mathbf{f}}\\ \vdots\end{bmatrix}\Big[\,\mathbf{F}\,\Big]\,. \tag{7}$$

The images $\mathbf{M}(\mathbf{x})$ and $\mathbf{F}(\mathbf{x})$ scale the respective source wavelets to generate the external sources $\underline{\mathbf{m}}(\mathbf{x},t)$ and $\mathbf{f}(\mathbf{x},t)$ for wavefield extrapolation. We solve equations 1 and 2 using the finite-difference representation of the time-derivative leading to the recursive relations for stress

$$\underline{\mathbf{t}} = \underline{\underline{\mathbf{c}}}\,\mathbf{H}\,\mathbf{u} + \mathbf{M}\,\mathrm{s}^{\mathbf{m}} \tag{8}$$

and particle displacement

$$\mathbf{u}_+ = 2\mathbf{u} + \frac{\Delta t^2}{\rho}\left(\nabla\cdot\underline{\mathbf{t}} + \mathbf{F}\,\mathrm{s}^{\mathbf{f}}\right) - \mathbf{u}_-\,. \tag{9}$$

These recursive equations allow us to compute the subsequent time wavefield $\mathbf{u}_+$ from wavefields at the current time $\mathbf{u}$ and at preceding time $\mathbf{u}_-$. In matrix form, we express the recurrent equations 8 and 9 as

$$\left[\begin{array}{c|cccc}\mathbf{I} & -\underline{\underline{\mathbf{c}}}\,\mathbf{H}\,\mathbf{I} & & & \\ \hline & -\frac{2\rho}{\Delta t^2} & \frac{\rho}{\Delta t^2} & 0 & \cdots\\ -(\nabla\cdot)\,\mathbf{I} & \frac{\rho}{\Delta t^2} & -\frac{2\rho}{\Delta t^2} & \frac{\rho}{\Delta t^2} & \cdots\\ & 0 & \frac{\rho}{\Delta t^2} & -\frac{2\rho}{\Delta t^2} & \cdots\\ & \vdots & \vdots & \vdots & \ddots\end{array}\right]\left[\begin{array}{c}\underline{\mathbf{t}}_0\\ \underline{\mathbf{t}}_1\\ \underline{\mathbf{t}}_2\\ \vdots\\ \hline \mathbf{u}_0\\ \mathbf{u}_1\\ \mathbf{u}_2\\ \vdots\end{array}\right] = \left[\begin{array}{c}\underline{\mathbf{m}}_0\\ \underline{\mathbf{m}}_1\\ \underline{\mathbf{m}}_2\\ \vdots\\ \hline \mathbf{f}_0\\ \mathbf{f}_1\\ \mathbf{f}_2\\ \vdots\end{array}\right] \tag{10}$$

where $\underline{\mathbf{m}}$ and $\mathbf{f}$ are the input wavefields, i.e., the source, and $\underline{\mathbf{t}}$ and $\mathbf{u}$ are propagating wavefields. We solve for $\underline{\mathbf{t}}$ and $\mathbf{u}$ from the top, i.e., forward in time, using the moment tensor and the body force sources. The forward operator takes a wavefield $\mathbf{d} = [\,\underline{\mathbf{m}}, \mathbf{f}\,]$ and generates a wavefield $\mathbf{w} = [\,\underline{\mathbf{t}}, \mathbf{u}\,]$ by propagating forward in time:

$$\mathbf{L}\mathbf{w} = \mathbf{d}\,. \tag{11}$$

The adjoint operator takes the wavefield $\mathbf{w} = [\,\underline{\mathbf{t}}, \mathbf{u}\,]$ and generates the adjoint wavefield $\mathbf{d}^* = [\,\underline{\mathbf{m}}^*, \mathbf{f}^*\,]$ by propagating backward in time:

$$\mathbf{w} = \mathbf{L}^{\dagger}\mathbf{d}^*\,. \tag{12}$$

In matrix form, we can write equation 12 as

$$\left[\begin{array}{c|c} \mathbf{I} & -\left(\nabla\cdot\right)^{\dagger}\,\mathbf{I} \\ \hline -\mathbf{H}^{\dagger}\,\underline{\underline{\mathbf{c}}}\,\mathbf{I} & \begin{array}{cccc} -\frac{2\rho}{\Delta t^2} & \frac{\rho}{\Delta t^2} & 0 & \cdots \\ \frac{\rho}{\Delta t^2} & -\frac{2\rho}{\Delta t^2} & \frac{\rho}{\Delta t^2} & \cdots \\ 0 & \frac{\rho}{\Delta t^2} & -\frac{2\rho}{\Delta t^2} & \cdots \\ \vdots & \vdots & \vdots & \ddots \end{array} \end{array}\right] \left[\begin{array}{c} \underline{\mathbf{m}}_0^* \\ \underline{\mathbf{m}}_1^* \\ \underline{\mathbf{m}}_2^* \\ \vdots \\ \hline \mathbf{f}_0^* \\ \mathbf{f}_1^* \\ \mathbf{f}_2^* \\ \vdots \end{array}\right] = \left[\begin{array}{c} \underline{\mathbf{t}}_0 \\ \underline{\mathbf{t}}_1 \\ \underline{\mathbf{t}}_2 \\ \vdots \\ \hline \mathbf{u}_0 \\ \mathbf{u}_1 \\ \mathbf{u}_2 \\ \vdots \end{array}\right] . \tag{13}$$

We solve for $\underline{\mathbf{m}}^*$ and $\mathbf{f}^*$ from the bottom, i.e., backward in time, using the sources $\underline{\mathbf{t}}$ and $\mathbf{u}$. The time reversal iterative equation for the adjoint strain is

$$\underline{\mathbf{m}}^* = \left(\nabla\cdot\right)^{\dagger}\,\mathbf{f}^* + \underline{\mathbf{t}} \tag{14}$$

and the adjoint particle displacement is

$$\mathbf{f}_-^* = 2\mathbf{f}^* + \frac{\Delta t^2}{\rho}\left(\mathbf{H}^{\dagger}\,\underline{\underline{\mathbf{c}}}\,\underline{\mathbf{m}}^* + \mathbf{u}\right) - \mathbf{f}_+^* , \tag{15}$$

where $\underline{\mathbf{m}}^*$ denotes the adjoint strain and $\mathbf{f}^*$ is the adjoint particle displacement. Finally, we obtain the respective adjoint source mechanism image using the adjoint fields as zero lag crosscorrelation with the moment tensor source wavelet

$$\left[\mathbf{M}^*\right] = \left[\begin{array}{cccc} \mathrm{s}_0^{\mathbf{m}} & \mathrm{s}_1^{\mathbf{m}} & \mathrm{s}_2^{\mathbf{m}} & \cdots \end{array}\right] \left[\begin{array}{c} \underline{\mathbf{m}}_0^* \\ \underline{\mathbf{m}}_1^* \\ \underline{\mathbf{m}}_2^* \\ \vdots \end{array}\right] \tag{16}$$

and the body force source wavelet

$$\left[\mathbf{F}^*\right] = \left[\begin{array}{cccc} \mathrm{s}_0^{\mathbf{f}} & \mathrm{s}_1^{\mathbf{f}} & \mathrm{s}_2^{\mathbf{f}} & \cdots \end{array}\right] \left[\begin{array}{c} \mathbf{f}_0^* \\ \mathbf{f}_1^* \\ \mathbf{f}_2^* \\ \vdots \end{array}\right] . \tag{17}$$

We represent the forward cascading operations in equations 6, 7 and 10 through forward operator

$$\mathbf{G}\mathbf{n} = \quad \mathbf{w} \tag{18}$$

and the equivalent adjoint cascading operations in equations 13, 16 and 17 by the adjoint operator

$$\mathbf{n} = \mathbf{G}^{\dagger}\mathbf{w} . \tag{19}$$

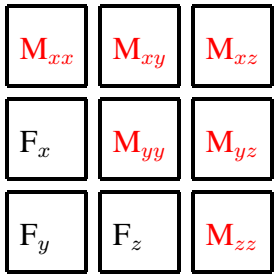
The forward operator $\mathbf{G}$ generates data $\mathbf{w}$ comprising of stress $\underline{\mathbf{t}}$ and particle displacement $\mathbf{u}$ from source mechanism image $\mathbf{n}$ of moment tensor $\mathbf{M}$ and body force $\mathbf{F}$ sources. The adjoint operator $\mathbf{G}^{\dagger}$ forms an image representing the source mechanism and is analogous to the gradient for the centroid-moment tensor inversion method (Kim et al., 2011). Since we formulate both the forward (equation 18) and adjoint (equation 19) operations, we can perform least-squares imaging to obtain high-resolution source mechanism images as

$$\mathbf{n} = \left(\mathbf{G}^{\dagger}\mathbf{G}\right)^{-1}\mathbf{G}^{\dagger}\mathbf{w} . \tag{20}$$

We can interpret $\mathbf{G}^{\dagger}\mathbf{G}$ as a point spread function (PSF) that blurs (via convolution) the image $\mathbf{n}$. Least-squares imaging deconvolves the PSF to generate high-resolution images.

3 NUMERICAL EXAMPLES

To analyze the theoretical performance of our proposed method, we perform a passive seismic numerical simulation with full aperture geometry. This ideal coverage enables us to discount the possibility of truncation artifacts through inadequate wavefield sampling to impair our analysis. We also show analysis of our technique with surface seismic acquisition to demonstrate the feasibility of our technique in a realistic scenario. The following examples cover reverse-time migrations and least-squares solutions. We present the source mechanism images using the tensor-vector matrix layout



,

which combines the stress tensor (in red) in its natural matrix representation together with the particle displacement vector wavefield in a combined 3×3 plot.

We set up our perfect aperture experiment using a constant elastic model with the source (in red) and spherical receiver (in black) geometry in Figure 1(a), emulating a passive seismic example. Note that the receivers are nearly evenly distributed on the sphere using a Fibonacci lattice (González, 2010). Table 1 represents the six different combinations of source mechanisms for analysis using the same acquisition geometry. Table 1 shows a summary of the figures and the corresponding source mechanisms. The image consists of three different slices of the 3D cube along the principal axes centered at the source location.

The first experiment in Table 1 resembles a double-couple earthquake source in the xz-plane. Figure 2 shows nine panels that populate the moment tensor matrix $(\mathrm{M}_{xx}, \mathrm{M}_{yy}, \mathrm{M}_{zz}, \mathrm{M}_{yz}, \mathrm{M}_{xz}, \mathrm{M}_{xy})$ and the body force vector $(\mathrm{F}_x, \mathrm{F}_y, \mathrm{F}_z)$. We observe components of source image that are symmetric in some axes, i.e., the image panel of F_x along the vertical axis or the image panel of F_z along the horizontal axis. However, of particular interest is the image panel of M_{xz} that is symmetric along both major axes which coincide with our exact source mechanism at $\mathrm{M}_{xz} = -1$ as the only nonzero component. The negative blue dot in panel

Experiment	$\mathbf{M}_{xx}$	$\mathbf{M}_{yy}$	$\mathbf{M}_{zz}$	$\mathbf{M}_{yz}$	$\mathbf{M}_{xz}$	$\mathbf{M}_{xy}$	$\mathbf{F}_x$	$\mathbf{F}_y$	$\mathbf{F}_z$
1	0	0	0	0	0	-1	0	0	0
2	1	1	1	0	0	0	0	0	0
3	0	0	0	0	0	0	0	0	1

Table 1. Summary of all the 3D source mechanism experiment.

	$\mathbf{M}_{xx}$	$\mathbf{M}_{yy}$	$\mathbf{M}_{zz}$	$\mathbf{M}_{yz}$	$\mathbf{M}_{xz}$	$\mathbf{M}_{xy}$	$\mathbf{F}_x$	$\mathbf{F}_y$	$\mathbf{F}_z$
symmetry	no	no	no	no	yes	no	no	no	no
values	0	0	0	0	1	0	0	0	0

Table 2. xz-plane double-couple source mechanism and image symmetry comparison.

$\mathbf{M}_{xz}$ shows the source location. Table 2 shows a summary of the image symmetry with the corresponding elements of the source mechanism. We obtain higher resolution source mechanism images through the least-squares formulation in equation 20. Comparing Figure 2 to Figure 3, the least-squares images are sharper and provide a more compact representation of the source image due to the removal of the PSF blurring effect. For the remaining examples, we focus on the source images from least-squares.

We demonstrate the ability of our method to identify source mechanism with multiple nonzero components such as an explosion. The source images in Figure 4 that display symmetry are on the main diagonal of the moment tensor images that indicates an explosive source. The source images consist of stacked spheres along the components associated with the principal axis, i.e., $\mathbf{M}_{xx}$, $\mathbf{M}_{yy}$, and $\mathbf{M}_{zz}$ along x-, y-, and z-axis respectively. Besides that, we perform least-squares imaging on body force source such as a seismic vibrator source. In Figure 5, we use a vertical body force as our source mechanism. The only panel that show symmetry is $\mathbf{F}_z$ which shows the capability of our method to identify both moment tensor and body force sources. This is important for scenarios where the recorded data is insufficient to describe the moment tensor source, we can describe them through its body force equivalent.

We repeat surface receivers (Figure 1(b)) to demonstrate our method with using surface monitoring methods to test the robustness against wavefield truncation artifacts. The limited aperture which translate to inadequate sampling of the wavefield may lead to inaccurate identification of the source mechanism from the artifacts. However, we demonstrate the robustness of our method through least-squares to minimize artifacts. For comparison with the full aperture scenario, we use the same double-couple earthquake source example in Figure 2 but acquired using surface receivers. The least-squares solution in Figure 6 shows that only panel $\mathbf{M}_{xz}$ describes the symmetry for source mechanism identification, although a reduction in compactness of the source image due to the limited aperture of a single-sided illumination from the top.

4 DISCUSSION

We demonstrate the ability to locate and identify the seismic source mechanism accurately. Since our formulation is derived from the elastic anisotropic wave equation, our method can be applied to media of arbitrary anisotropy and heterogeneity given the media parameters are known (also a requirement for any other wavefield-based method). The source mechanism imaging method provides a fast and robust way to obtain the source parameters without the need for lengthy iterative inversion. However, to reduce aperture and source wavelet related artifacts, we are required to perform least-squares imaging that would increase the computational cost. Our imaging method and conventional inversion-based methods are related in that the source images form the gradient for waveform inversions. The imaging condition in equation 16 is comparable to the moment tensor gradient defined from the Fréchet derivatives by Kim et al. (2011) in their centroid-moment tensor inversion method. Besides the moment tensor image, our method also provides the body force image which is essential when the observed data are not capable to not fully describe the moment tensor source. A natural extension of our approach is to use all of the source images (**M** and **F**) to perform waveform-based inversion to obtain medium parameters. The least-squares imaging provides high-resolution source images, and could accelerate waveform inversions.

5 CONCLUSIONS

We demonstrate a wavefield-based imaging method that can robustly and accurately locate seismic sources and identify its mechanism. Our technique requires both stress and particle displacement data, but can be formulated using either stress or particle displacement as special cases. This methodology leverages strain and displacement acquisition using novel multicomponent DAS acquisition. Our source images naturally identify the source mechanism as they are individual images for the respective moment tensor and body force components. The ability to obtain the source location and mechanism without the need for lengthy iterative processes could potentially allow practitioners to make timely decisions about the reservoirs for immediate business impact. Our method using the least-squares solution facilitates fast and accurate waveform inversion for source and medium parameters. The methodology presented in this paper applies to media of arbitrary anisotropy and heterogeneity.

6 ACKNOWLEDGMENTS

We would like to thank the sponsors of the Center for Wave Phenomena, whose support made this research possible and Oscar Jarillo Michel for fruitful discussions. The reproducible

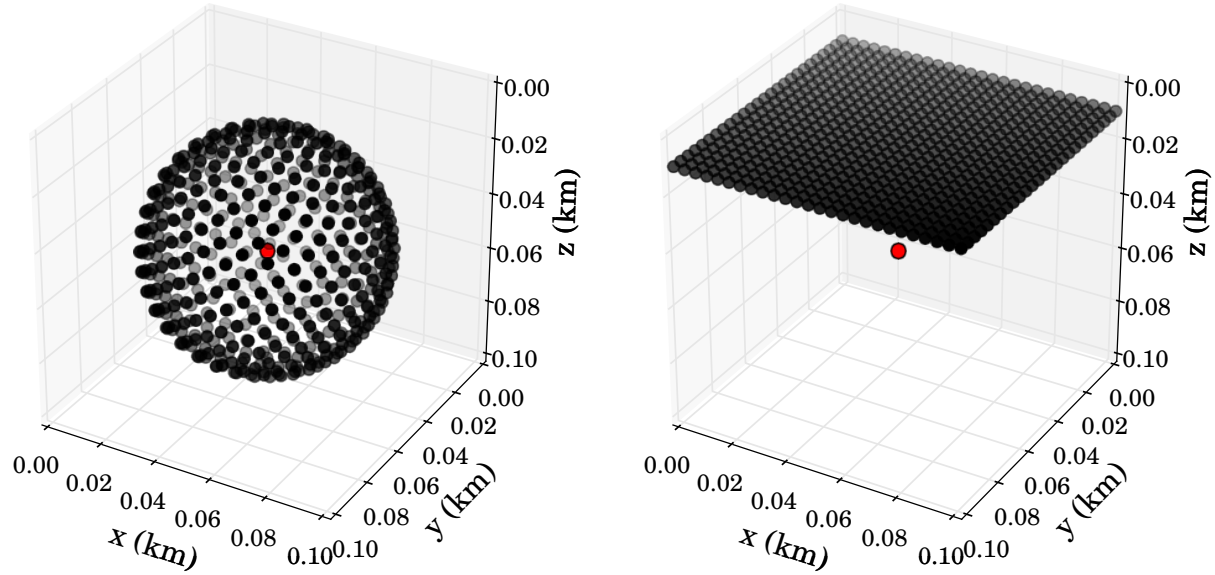


Figure 1. 3D microseismic experiment setup with receivers providing (a) ideal spherical coverage and (b) surface seismic acquisition. The red dot represents the source location.

numeric examples in this paper use the Madagascar open-source software package (Fomel et al., 2013) freely available from http://www.ahay.org.

REFERENCES

Aki, K., and P. G. Richards, 2002, Quantitative seismology.

Artman, B., I. Podladtchikov, and B. Witten, 2010, Source location using time-reverse imaging: Geophysical Prospecting, **58**, 861–873.

Baig, A., and T. Urbancic, 2010, Microseismic moment tensors: A path to understanding frac growth: The Leading Edge, **29**, 320–324.

Bazargani, F., and R. Snieder, 2015, Optimal source imaging in elastic media: Geophysical Journal International, **204**, 1134–1147.

Chambers, K., B. D. Dando, G. A. Jones, R. Velasco, and S. A. Wilson, 2014, Moment tensor migration imaging: Geophysical Prospecting, **62**, 879–896.

Fomel, S., P. Sava, I. Vlad, Y. Liu, and V. Bashkardin, 2013, Madagascar: open-source software project for multidimensional data analysis and reproducible computational experiments: Journal of Open Research Software, **1**.

Fukahata, Y., Y. Yagi, and L. Rivera, 2013, Theoretical relationship between back-projection imaging and classical linear inverse solutions: Geophysical Journal International, **196**, 552–559.

Gharti, H. N., V. Oye, D. Kühn, P. Zha, et al., 2011, Simultaneous microearthquake location and moment-tensor estimation using time-reversal imaging: 81st Annual International Meeting, SEG, Expanded Abstracts, 1632–1637.

González, Á., 2010, Measurement of areas on a sphere using Fibonacci and latitude–longitude lattices: Mathematical Geosciences, **42**, 49.

Jarillo Michel, O., and I. Tsvankin, 2014, Gradient calculation for waveform inversion of microseismic data in VTI media: Journal of Seismic Exploration, **23**, 201–207.

———, 2015, Estimation of microseismic source parameters by 2D anisotropic waveform inversion: Journal of Seismic Exploration, **24**, no. 5, 379–400.

———, 2017, Waveform inversion for microseismic velocity analysis and event location in VTI media: Geophysics, **82**, WA95–WA103.

Kawakatsu, H., and J.-P. Montagner, 2008, Time-reversal seismic-source imaging and moment-tensor inversion: Geophysical Journal International, **175**, 686–688.

Kim, Y., Q. Liu, and J. Tromp, 2011, Adjoint centroid-moment tensor inversions: Geophysical Journal International, **186**, 264–278.

Li, L., I. Abakumov, H. Chen, X. Wang, D. Gajewski, et al., 2017, Comparison and generalization of correlation-based seismic source imaging methods: 87th Annual International Meeting, SEG, Expanded Abstracts, 2913–2917.

Lim Chen Ning, I., and P. Sava, 2016, Multicomponent distributed acoustic sensing: 86th Annual International Meeting, SEG, Expanded Abstracts, 5597–5602.

———, 2017, High-resolution multicomponent distributed acoustic sensing: 87th Annual International Meeting, SEG, Expanded Abstracts, 941–946.

———, 2018, Multicomponent distributed acoustic sensing:

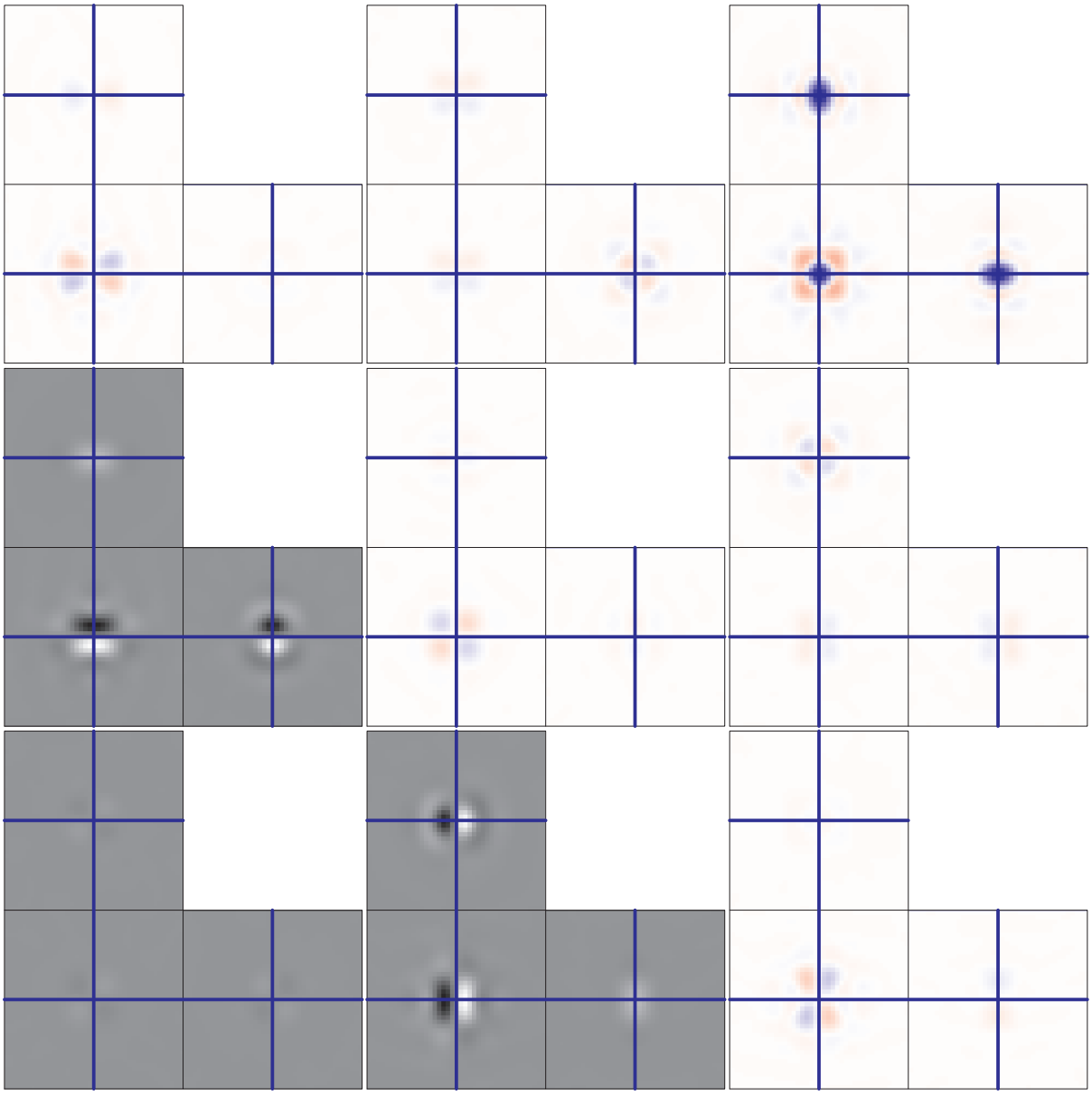


Figure 2. Source mechanism reverse time migration using the experiment setup in Figure 1(a) with seismic moment tensor $\mathbf{M} = \{\mathbf{0}, \mathbf{0}, \mathbf{0}, \mathbf{0}, \mathbf{0}, -\mathbf{1}\}$.

Concept and theory: Geophysics, **83**, P1–P8.

Maxwell, S. C., J. Rutledge, R. Jones, and M. Fehler, 2010, Petroleum reservoir characterization using downhole microseismic monitoring: Geophysics, **75**, 75A129–75A137.

Montagner, J.-P., C. Larmat, Y. Capdeville, M. Fink, H. Phung, B. Romanowicz, E. Clévédé, and H. Kawakatsu, 2012, Time-reversal method and cross-correlation techniques by normal mode theory: a three-point problem: Geophysical Journal International, **191**, 637–652.

Nakahara, H., and M. M. Haney, 2015, Point spread functions for earthquake source imaging: An interpretation based on seismic interferometry: Geophysical Journal International, **202**, 54–61.

Tromp, J., C. Tape, and Q. Liu, 2005, Seismic tomography, adjoint methods, time reversal and banana-doughnut kernels: Geophysical Journal International, **160**, 195–216.

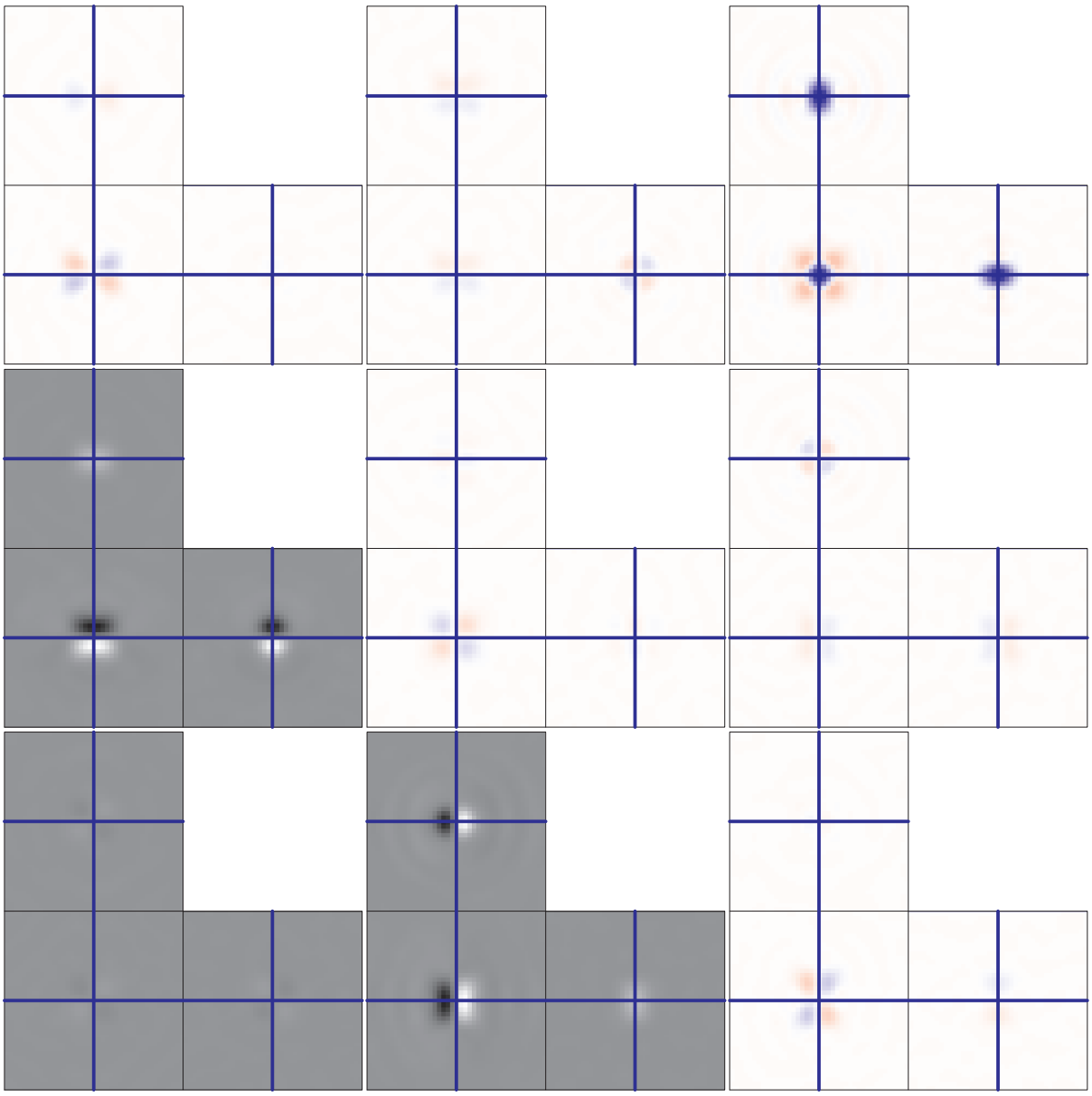


Figure 3. Source mechanism **Least-squares** reverse time migration corresponding to the images in Figure 2 with seismic moment tensor $\mathbf{M} = \{\mathbf{0}, \mathbf{0}, \mathbf{0}, \mathbf{0}, \mathbf{0}, -\mathbf{1}\}$.

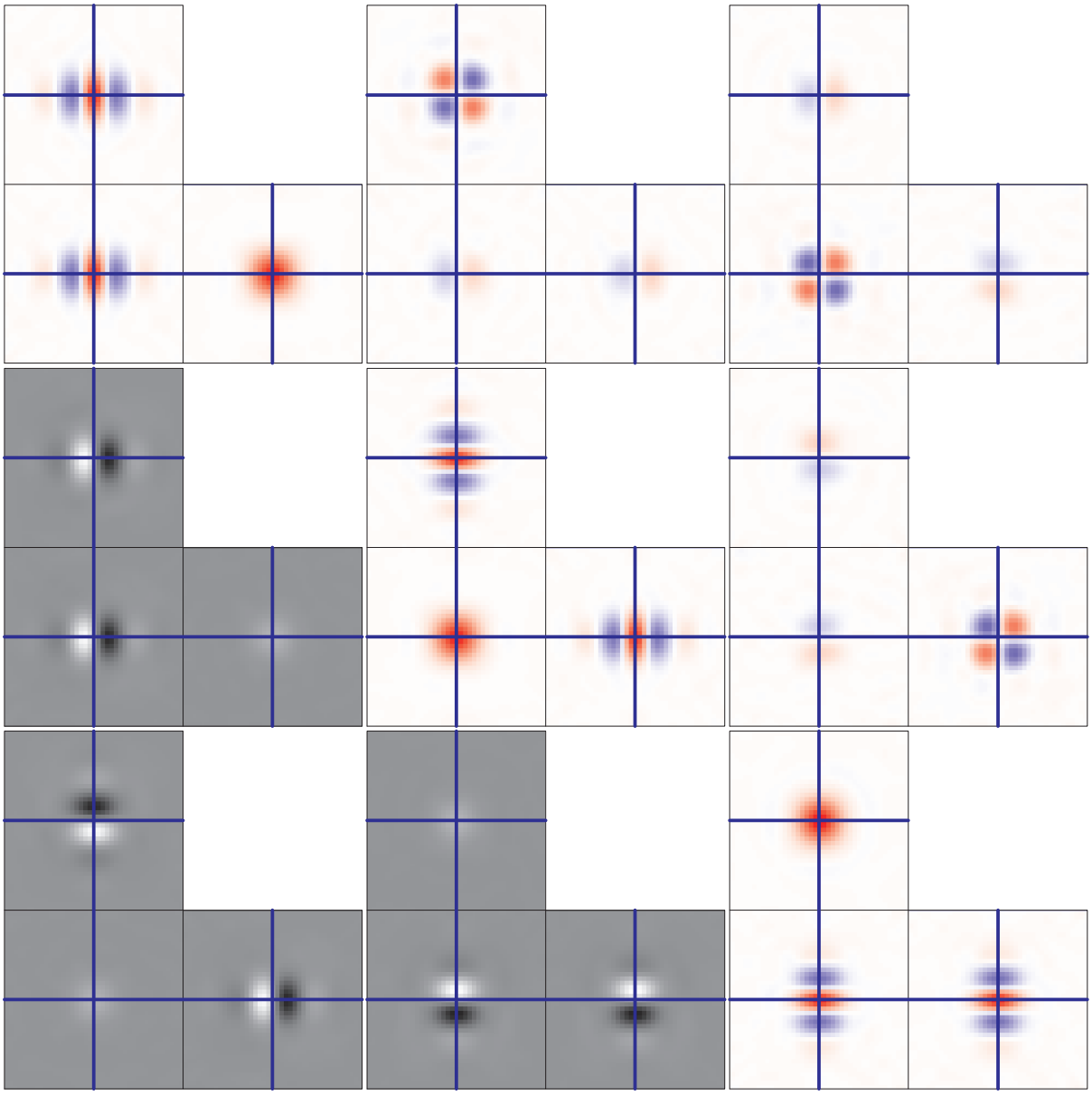


Figure 4. Source mechanism **Least-squares** reverse time migration for seismic moment tensor $\mathbf{M} = \{\mathbf{1}, \mathbf{1}, \mathbf{1}, \mathbf{0}, \mathbf{0}, \mathbf{0}\}$.

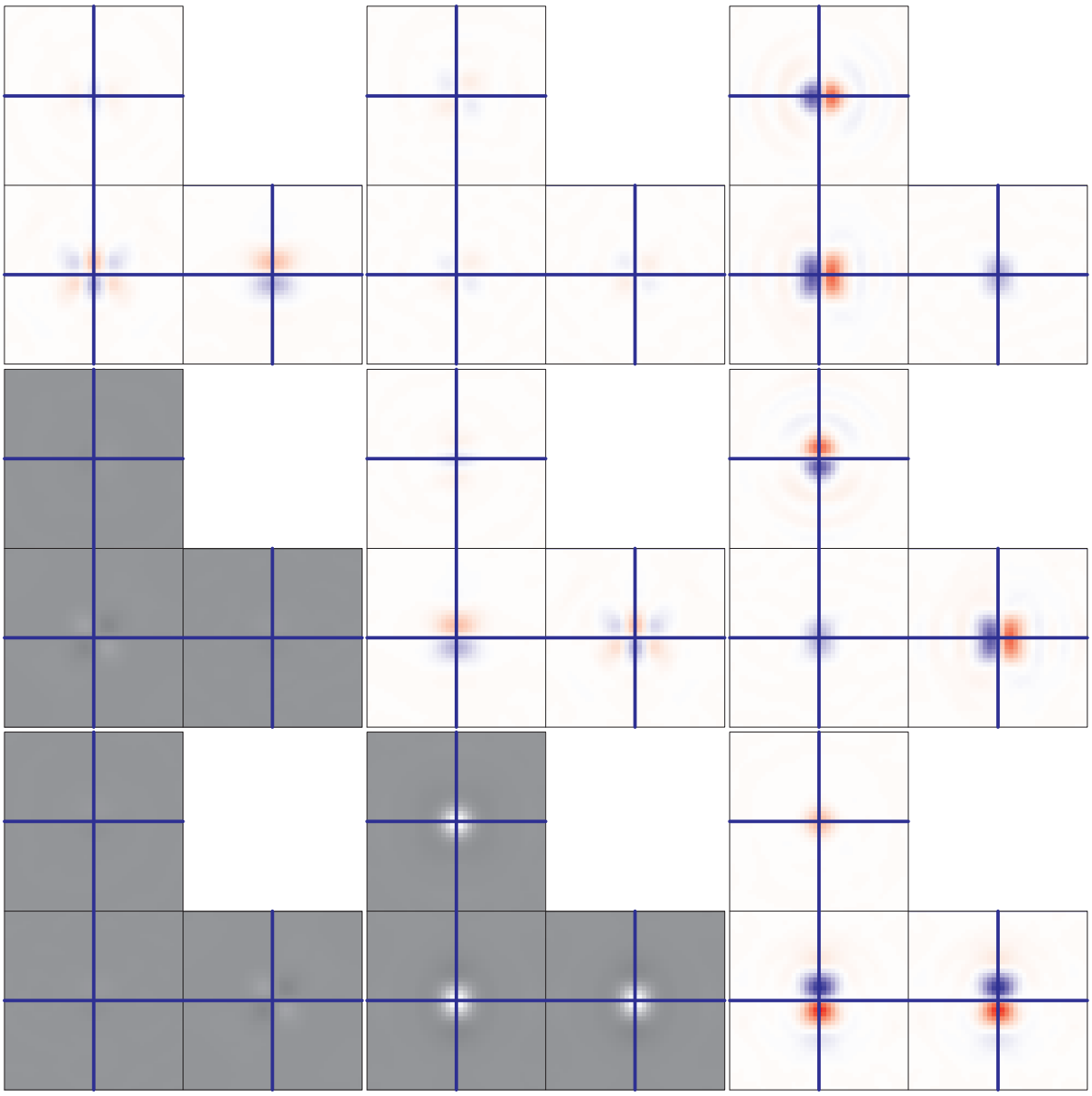


Figure 5. Source mechanism **Least-squares** reverse time migration for body force vector $\mathbf{F} = \{\mathbf{0}, \mathbf{0}, \mathbf{1}\}$.

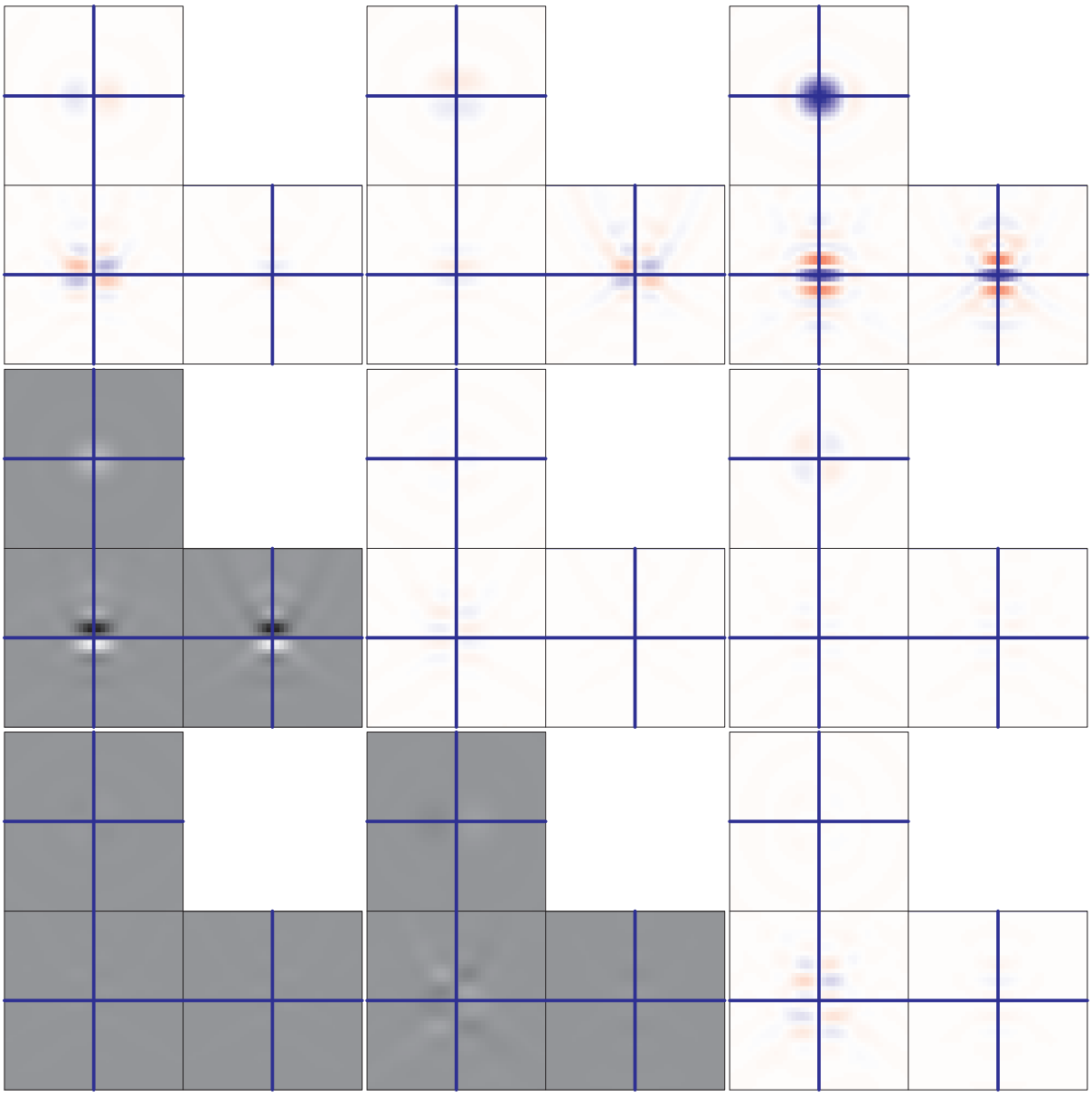


Figure 6. Source mechanism **Least-squares** reverse time migration using the surface seismic acquisition geometry in Figure 1(b) for seismic moment tensor $\mathbf{M} = \{\mathbf{0}, \mathbf{0}, \mathbf{0}, \mathbf{0}, \mathbf{0}, -\mathbf{1}\}$.